Carbon Nanotube Supported Fluorine Substituted Iron Phthalocyanine Enabling Boosted Polysulfide Redox Conversion Kinetics and Cyclic Stability

Jiaqi Zhao,[a] Zhanwei Xu,*[a] Yujiao Zhang, [b] Qingzhu Jin,[a] Longhua Guo,[a] Siyu Chen,[d] Xuetao Shen, [a] Jiayin Li, [a] Zhi Li,*[a][c]

[a] JQ. Zhao, Dr.ZW. Xu, LH. Guo, Dr. XT. Shen, Dr. JY. Li, Prof. Z Li,
Shaanxi Key Laboratory of Green Preparation and Functionalization for Inorganic Materials,
Shaanxi University of Science and Technology,
Xi'an, 710021, PR China
E-mail: xuzhanwei@sust.edu.cn, zhi.li@ualberta.ca

[b] YJ. Zhang,
Ramu NiCo Management (MCC) Limited
Shuguangxili, Chaoyang District
Beijing 100028, PR China

[c] Prof. Z Li
National Institute for Nanotechnology (NINT)
National Research Council of Canada Edmonton
Alberta T6G 2 M9, Canada

[d] SY. Chen
Catalan Institute of Nanoscience and Nanotechnology (ICN2)
Campus UAB, Bellaterra
08193 Barcelona, Spain

Abstract: The sluggish transition and shuttle of polysulfides (LiPS) significantly hinder the application and commercialization of Li-S batteries. Herein, carbon nanotubes (CNTs) supported 10 nm sized iron Hexadecafluorophthalocyanine ($FePcF_{16}$/CNTs) are prepared using a solid synthesis approach. The well-exposed $FePcF_{16}$ molecular improve the LiPS capture efficiency and redox kinetics by its central Fe-N_4 units and F functional groups. The strong electron withdraw F groups significantly promote the conjugate effect and decrease the steric hinderance during mass migration procedure. Distribution of relaxation time (DRT) analysis shows that the Fe-N_4 units exhibit strong affinity towards LiPS and the F groups further improve the Li^+ diffusion rate in Li_2S nucleation and oxidation procedure, accomplishing a porous surface on cathode. As a result, the $FePcF_{16}$/CNTs separator exhibits a high initial capacity of 1136.2 mAh g^{-1} at 0.2C, excellent rate capacity of 624.9 mAh g^{-1} at 5C and superior long-term stability at 2C surviving 300 cycles with a low capacity decay of 0.43‰.

Introduction

Lithium sulfur batteries (LSBs) are regarded as the most promising energy storage systems, due to their high theoretical capacity (1675 mAh g^{-1}), low cost and sufficient resources of cathode material sulfur[1]. However, Sulfur reduction reaction in ether-based electrolyte becomes very complex[2]. Before totally reduced to Li_2S, active sulfur converts into a series of intermediate lithium polysulfides (LiPS), besides Li_2S_8, Li_2S_6, Li_2S_4, Li_2S_2[3]. However, some of LiPS can dissolve in electrolyte as well as shuttle to the anode side due to the concentration gradient and causes the formation of 'dead' sulfur[4]. The sluggish conversion kinetics of LiPS and intrinsic low conductivity of all S species also cause the residual of LiPS in electrolyte indirectly[5]. LSBs exhibits steel capacity decay along with poor cycle stability and awful rate performance in practical application[6].

Lots of strategies have been devoted to alleviating the shuttle effect [7]. Functional modification materials are usually regarded as the most effective strategy to improve batteries performance. To achieve electronic conductivity and LiPS catalyzation, carbon supported transition metal compounds, such as MoS_2[8], CoS_2[9], MoN[10], MoO_2[11], CeO_2[12], TiO_2[13] et al, are widely used as separator modification materials by capturing the LiPS with formed M-S bond and catalyzing the LiPS conversion kinetics. However, specific catalytic lattice interface and limited catalytic active sites still hinder the redox efficiency of LiPS conversion[14].

Metal phthalocyanines (MPc) have widely known due to its macro ring conjugated structure and M-N_4 catalytic center[15]. The conjugated effect makes MPc are easily gain as well as lose electron in both reduction and oxidation reaction, indicating a matched redox kinetics[16]. Furthermore, lots of works have proved that the central M-N_4 units can accelerate the conversion kinetics of LiPS by weakening the Li-S bond via strong adsorption[17].

Recent years, the derivations of MPc with substituent groups were reported in the past years, like -NH_2[17d], -Cl[17e], -F[17f], -NO_2[17g].The electron-rich F-substituted groups enhance the conjugate effect of MPc ring, further promoted the redox ability towards LiPSs conversion. And the extremely small atomic radius (0.079 nm) of F atoms reduce the steric hindrance during mass transfer procedure.

In this work, 10 nm sized iron hexadecafluorophthalocyanine was uniformly dispersed on the wall of carbon nanotubes ($FePcF_{16}$/CNTs) and used for catalyzing LiPS conversion in both reduction and oxidation reaction. With sixteen strong electron withdraw groups F in skeleton, $FePcF_{16}$ provides strong electrostatic affinity towards Li ion in charge/discharge process. The improved migration further decreases the electrochemical polarization. Ultra-fined $FePcF_{16}$ nanoparticles improve its active surface areal as well as expose more molecular catalytic sites. In addition, the introduced $FePcF_{16}$ changes the Li_2S precipitation morphology on cathode surface due to the enhanced mass migration rate. The porous Li_2S interlayer is accumulated by a bench of Li_2S nanospheres, large specific surface areal enables better contact of electrolyte and decreases the oxidation difficulty of Li_2S in subsequent cycles as well as an improved cycle stability. Hence the cell with the $FePcF_{16}$/CNTs exhibits excellent electrochemical performance with an initial capacity of 708.2 mAh g^{-1} at 2C, with a promising cycle stability and low capacity decay of 0.43‰ at 2C, and high rate performance of 624.9 mAh g^{-1} at 5C.

Results and Discussion

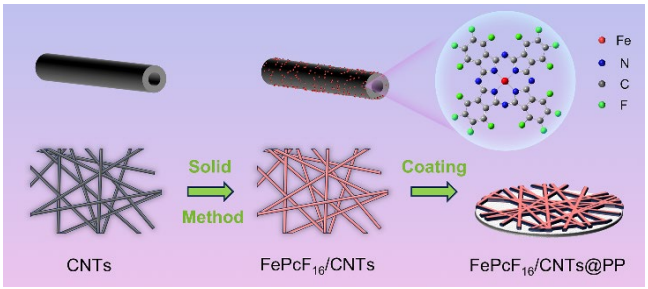

Scheme 1. Schematic diagram of synthesis for the $FePcF_{16}$/CNTs.

The $FePcF_{16}$/CNTs was prepared by one step solid phase reaction, which was illustrated in scheme 1 and detailed in Experimental Section. The SEM image in Figure 1a shows that the $FePcF_{16}$ nanoparticles are uniformly dispersed on the wall of CNT tubes. High magnification SEM image in Figure 1b reveals that lots of $FePcF_{16}$ nanoparticles with the size around 10 nm have been connected. In Figure 1c and Figure S1, the formed $FePcF_{16}$ anchored on the surface of CNTs, obviously. The HRTEM reveals that the lattice space of $FePcF_{16}$ and CNTs are 2.04 Å and 3.43 Å.

The FTIR spectra of $FePcF_{16}$/CNTs, $FePcF_{16}$ and CNTs were displayed in Figure 2g. the $FePcF_{16}$/CNTs and $FePcF_{16}$ exhibits the same characteristic peaks. The peaks around 646 cm^{-1} and 756 cm^{-1} are corresponding to the C-C out-of-plane ring deformation and C-N in-plane stretching vibration of the phthalocyanine ring, respectively. The peak around 856 cm^{-1} is attributed to the Fe ligand vibration in the central of the phthalocyanine. In around 1148 cm^{-1}, the peak is assigned to the C-F bond on the skeleton. The peaks around 1535 cm^{-1} and 1627cm^{-1} are corresponding to the C=N stretching and C=C macrocycle ring deformation.

The main Raman characteristic peaks of the $FePcF_{16}$/CNTs located in 1344 cm^{-1} and 1573 cm^{-1}. The peak at around 1344 cm^{-1} is overlapped by two peaks from the lattice defect of CNTs(1344 cm^{-1}) and the C-C pyrrole stetch of the $FePcF_{16}$(1340 cm^{-1})[18], respectively. And the peak at around 1573 cm^{-1} is assigned to valence vibrations of the C–C bond in CNTs[19]. And the characteristic peak of the $FePcF_{16}$ located in 1525.7 cm^{-1} was overlapped by the strong carbon peak at around 1573 cm^{-1} , belonging to the C-N aza-group stretch[20]. (Figure 2h).

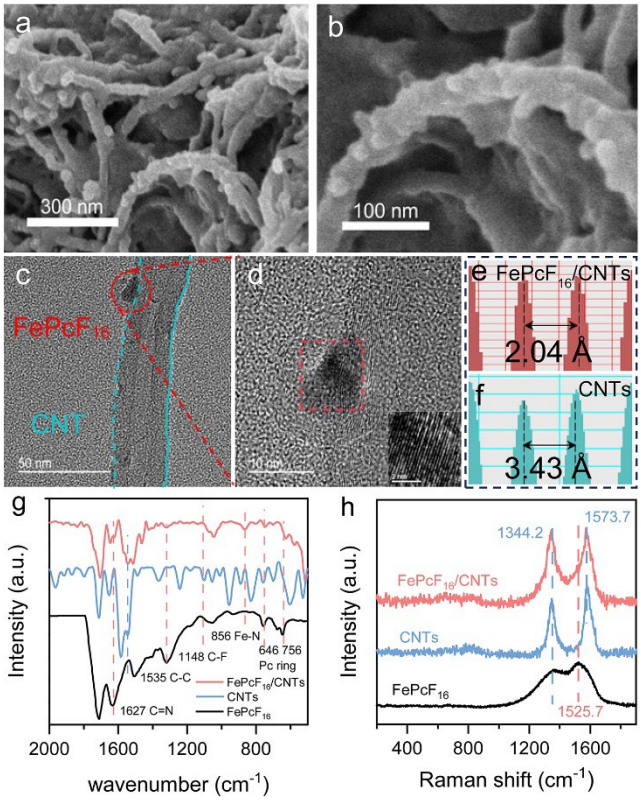

Figure 1. (a) and (b) SEM images of the $FePcF_{16}$/CNTs. (c) and (d) HRTEM images of the $FePcF_{16}$/CNTs, the lattice spacing of (e) $FePcF_{16}$ and (f) CNTs. (g) FTIR spectra of $FePcF_{16}$, CNTs and the $FePcF_{16}$/CNTs. (h) Raman spectra of $FePcF_{16}$, CNTs and the $FePcF_{16}$/CNTs.

Activation energy(E_a) is an important factor to insight the catalytic activity[22]. According to the Arrhenius equation, the LiPS conversion kinetics may be represented by E_a and the charge transfer resistance is correctly relate to kinetics. the EIS spectrums under corresponding potential were measured at various temperatures(Figure 2a and detailed in Figure S2). By fitting the charge transfer resistance verses temperatures, The E_a under different conversion step were obtained(Figure 2b)[22].

The E_a values at three typical charge/discharge state were displayed in figure 2c, the E_a at 2.10 V and 1.80 V are assigned to the transition from Li_2S_4 to Li_2S_2 on electrode surface and the solid-solid conversion from Li_2S_2 to Li_2S, respectively. In addition, the Li_2S activation procedure can be considered at 2.25 V. The $FePcF_{16}$/CNTs separator shows lowest E_a at three typical potential point of 0.13 eV, 0.21 eV and 0.23 eV, demonstrating that the introduction of the F functional groups can further

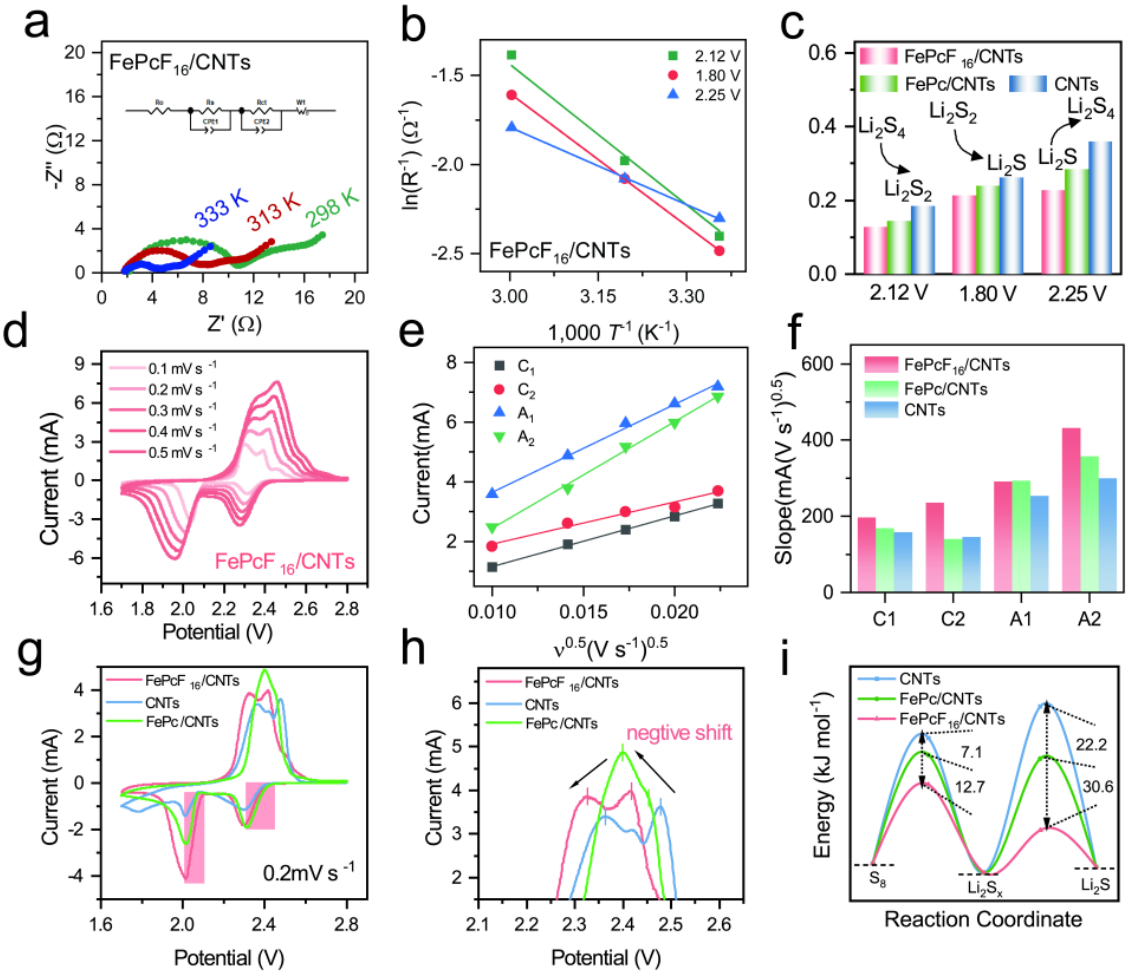

Figure 2 . (a) EIS spectra at 2.12 V under various temperatures, inset: simplified-contact Randles-equivalent circuit. (b) An Arrhenius plot for the linear relationship between logarithmic values of the reciprocal of charge transfer resistance and the reciprocal of absolute temperatures for 2.12 V, 1.80 V and 2.25 V. (c) The calculated E_a of the $FePcF_{16}$/CNTs and CNTs. (d) CV curves of the $FePcF_{16}$/CNTs separator under various scan rates. (e) Plot of the currents of all CV redox peaks versus the square root of the scan rates. (f) Slope values of the four peaks. (g) CV curves of the $FePcF_{16}$/CNTs. CNTS separators at 0.2 mV s^{-1}. (h) Partial CV curves of the $FePcF_{16}$/CNTs and CNTs separators. (i) the relative activation energy during different conversion processes with various separator.

reduces the E_a of LiPS conversion, which may be attribute to the change of surface electrostatic potential.

The mass transfer rate is an important part of the conversion kinetics. To insight the Li^+ diffusion coefficient (D_{Li+}). The CV curves of the $FePcF_{16}$/CNTs and CNTs separators under 0.1 ~ 0.5 mV s^{-1} scan rates were measured and displayed in Figure 2d and Figure S3a. The cell with the $FePcF_{16}$/CNTs separator shows a typical CV shape and lower potential difference between reduction peaks and oxidation peaks (detailed in Table S1) ,demonstrating the improved LiPS redox conversion kinetics and reduced electrochemical polarization.

The corresponding Li^+ diffusion coefficient of separators at various conversion procedure were displayed in Figure 2e and Figure S3c-3f. according to the equation (S1), the slope value is positively related to the D_{Li+}. The $FePcF_{16}$/CNTs exhibits higher slope values in all four redox peaks, indicating the Li^+ migration rate could be increased by the Fe-N_4 central units and intense electron withdraw groups F.

The CV curves at 0.2 mV s^{-1} were displayed in Figure 2g. The cell of the $FePcF_{16}$/CNTs shows much higher response currents than FePc/CNTs and CNTs separators in reduction peaks as well as obviously negative shift of oxidized peaks, indicating a boosted LiPS oxidation procedure. The oxidation peaks in Figure 2h shows an obvious shift towards lower potential, indicating the reduced oxidation potential. The corresponding tafel plots of peak C1 C2 are shown in Figure S4a and Figure S4b. The $FePcF_{16}$/CNTs separator exhibits lower tafel slope in all three peaks especially in the Li_2S nucleation (C2) and activation (A1), demonstrating the improved Li_2S redox kinetics. Furthermore, According to equation (S2) and the tafel slopes, the relative activation energy(ΔE_a) of three samples could be caculated[23]. For the reduction process of S_8 to Li_2S_x, the ΔE_{a1} values of the $FePcF_{16}$/CNTs, FePc/CNTs and CNTs separator are increased by 12.7 kJ mol^{-1} and 7.1 kJ mol^{-1}. The ΔE_{a2} values which corresponding to the procedure of Li_2S_x to Li_2S are increased by 30.6 kJ mol^{-1} and 22.2 kJ mol^{-1}. Above results demonstrate the

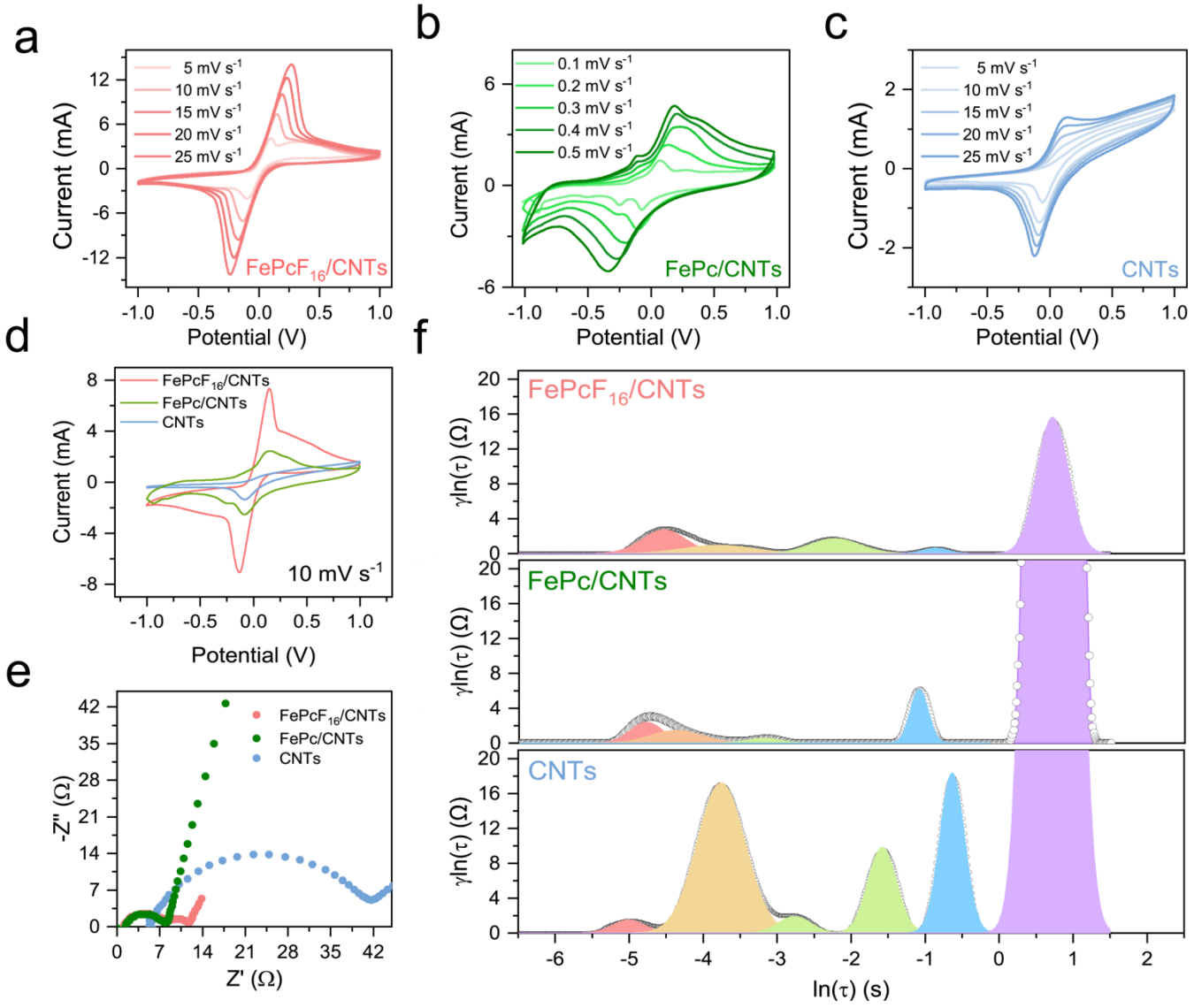

Figure 3. CV curves of symmetric cells with separators of (a) the $FePcF_{16}$/CNTs, (b) FePc/CNTs and (c) CNTs under various scan rates. (d) CV curves of the $FePcF_{16}$/CNTs, FePc/CNTs and CNTs separators at 10 mV s^{-1}. (e) EIS spectra of the symmetric cells with the $FePcF_{16}$/CNTs, FePc/CNTs and CNTs separators. (f) The DRT profile corresponding to EIS date of the $FePcF_{16}$/CNTs, FePc/CNTs and CNTs symmetric cells.

introduce of Fe-N_4 catalytic units and F functional groups can both reduce the formation energies of Li_2S_x and Li_2S.

The symmetric CV curves with the $FePcF_{16}$/CNTs, FePc/CNTs and CNTs cell under various scan rate were shown in Figure 3a, Figure 3b and Figure 3c. In the cell of CNTs separator, CV curves exhibits tiny current and asymmetric peak intensity. For comparison, the cell with FePc/CNTs separator exhibits an enhanced intensity of redox respond peaks than CNTs cell, which represents the introduced FePc could enhance both LiPS reduction and oxidation dynamics. Furthermore, the CVs of $FePcF_{16}$/CNTs depict high response currents in both reduction and oxidation symmetric peaks, indicating the introduced F functional group boost the Li_2S_6 conversion kinetics(Figure 3d)The EIS spectra of all three symmetric cells were shown in Figure 3e. The FePc/CNTs and $FePcF_{16}$/CNTs cell both cause an obvious reduction of semicircle (Rct) than CNTs. And the F functional group futher reduces the resistance in Li^+ diffusion procedure. Then the DRT analysis was used to reveal the overlapping electrochemical resistances[24]. A typical DRT curves could be distinguished into various regions with different time constant (the peak center), the integrate value of those peaks is the electrochemical resistance of various procedure(detailed in Figure S3e)[24,25].

The DRT curves of the $FePcF_{16}$/CNTs, FePc/CNTs and CNTs were displayed in Figure 3f. The intrinsic resistances of the $FePcF_{16}$/CNTs and FePc/CNTs at around -5 are a little larger than CNTs, this is attributed that the semiconductive $FePcF_{16}$ and FePc dispersed on the walls of CNTs. When introduce the FePc, the charge tranfer resistance and LiPS diffusion resistance reduce obviously via the central Fe-N_4 unit.

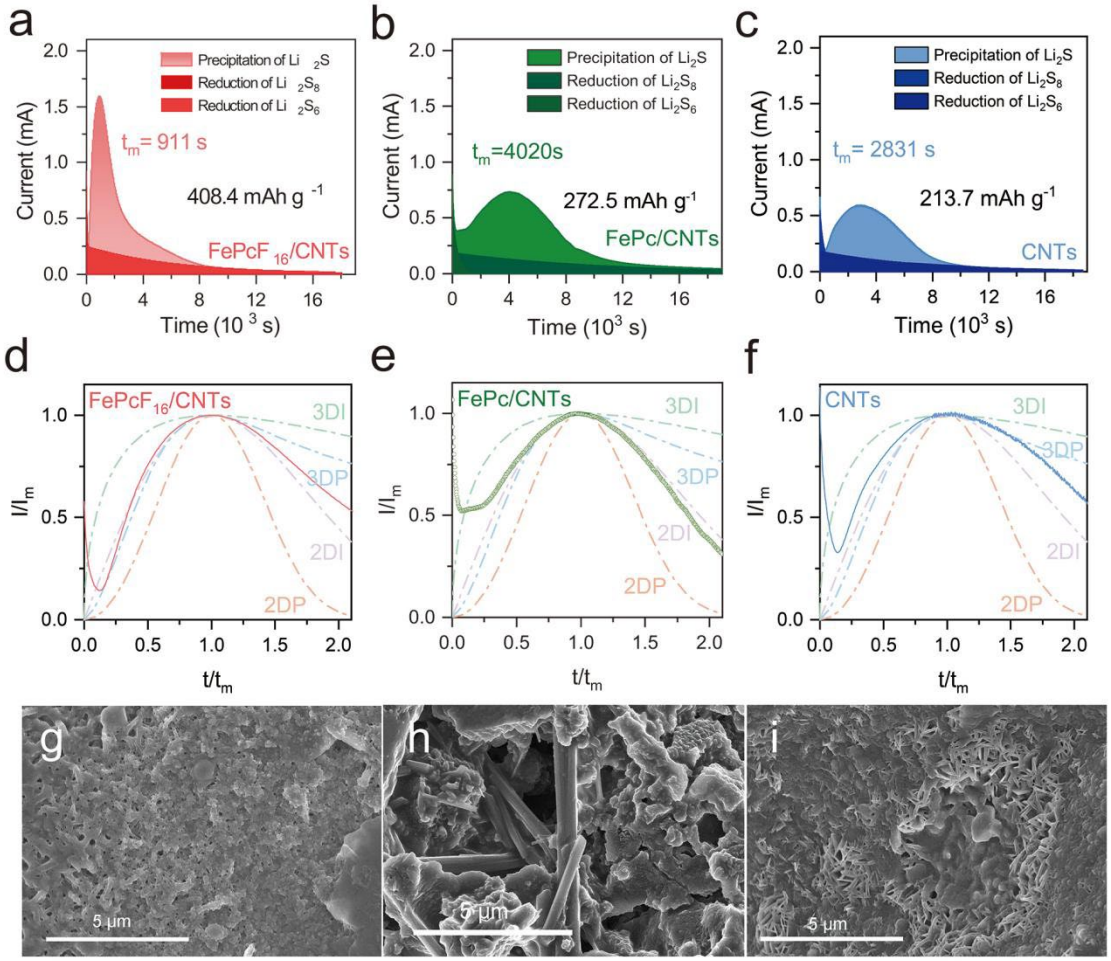

Figure 4 . Potentiastatic Li_2S deposition curves of (a) the $FePcF_{16}$/CNTs, (b) FePc/CNTs and (c) CNTs separator at 2.09 V. Corresponding dimensionless Current–time transients in comparison with theoretical models of (d) the $FePcF_{16}$/CNTs. (e) FePc/CNTs and (f) CNTs separator. SEM images of final Li_2S deposition morphology of (g) The $FePcF_{16}$/CNTs, (h) FePc/CNTs and (i) CNTs.

Furthermore, the strong electron withdraw F groups of the $FePcF_{16}$ unit enabled a promoted diffusion resistance both LiPS and Li^+, which can be proved by the reduction of P_2 P_3 and P_3' peaks.

To further illustrate liquid-solid tranfer performance of the $FePcF_{16}$/CNTs FePc/CNTs and CNTs interlayer, potentiostatic curve of the $FePcF_{16}$/CNTs, FePc/CNTs and CNTs separators were measured under 2.09 V, which is attributed to the Li_2S nucleation potential at 0.2 C[26] (Figure 4a, Figure 4b and Figure 4c). The $FePcF_{16}$/CNTs separator achieves a higher precipitation capacity of 408.4 mAh g^{-1}, higher than the FePc/CNTs (272.5 mAh g^{-1}) and CNTs (213.7 mAh g^{-1}). Additionally, the improved t_m shows the faster nucleation rate of the $FePcF_{16}$/CNTs, demonstrating the promoted conversion kinetics.

Current-Time transient were used to investigate the liquid solid transition behavior of the $FePcF_{16}$/CNTs, CNTs and PP separators[27]. based on the theoretical precipitation models from Beweick Fleischman Thirsk (BFT) model and Scharifker-Hills (SH) Model were delivered[28]. Four typical models are attributed to the lattice incorporation growth (2DI and 2DP) and the bulk diffusion controlled growth (3DI and 3DP) as well as the typical deposition morphology of 2D-plate like and 3D sphere like, respectively. The Current-time transients curve of FePc/CNTs is most corresponding to the 2DI model, which may growth 2D Li_2S.The curve of the $FePcF_{16}$/CNTs is correspond to the 2DI and 3DP hybrid behavior in both nucleation and growth process[29], which is similar to the curve of CNTs. Also, the highest t_m value suggests the highest nucleation rate than FePc/CNTs and CNTs separators (Figure 4d, Figure 4e and Figure 4f).

The SEM images of Li_2S morphology were shown in Figure 4g, Figure 4h and Figure 4i. The $FePcF_{16}$/CNTs exhibits an aggressive of Li_2S nanosphere surface morphology, the porous surface improves capacity by avoilding surface passivation and the loose Li_2S morphology enhances the subsequent oxidation behavior and sulfur utlization. For comparison, the Li_2S morphology in FePc/CNTs cell displays stick-like morphology in several micrometers. FePc/CNTs and CNTs separators delivered typical 2D plate-like, corresponding to the sluggish bulk diffusion dynamics. Additionally, CNTs separator further growth a passivation layer on the top of Li_2S plate.

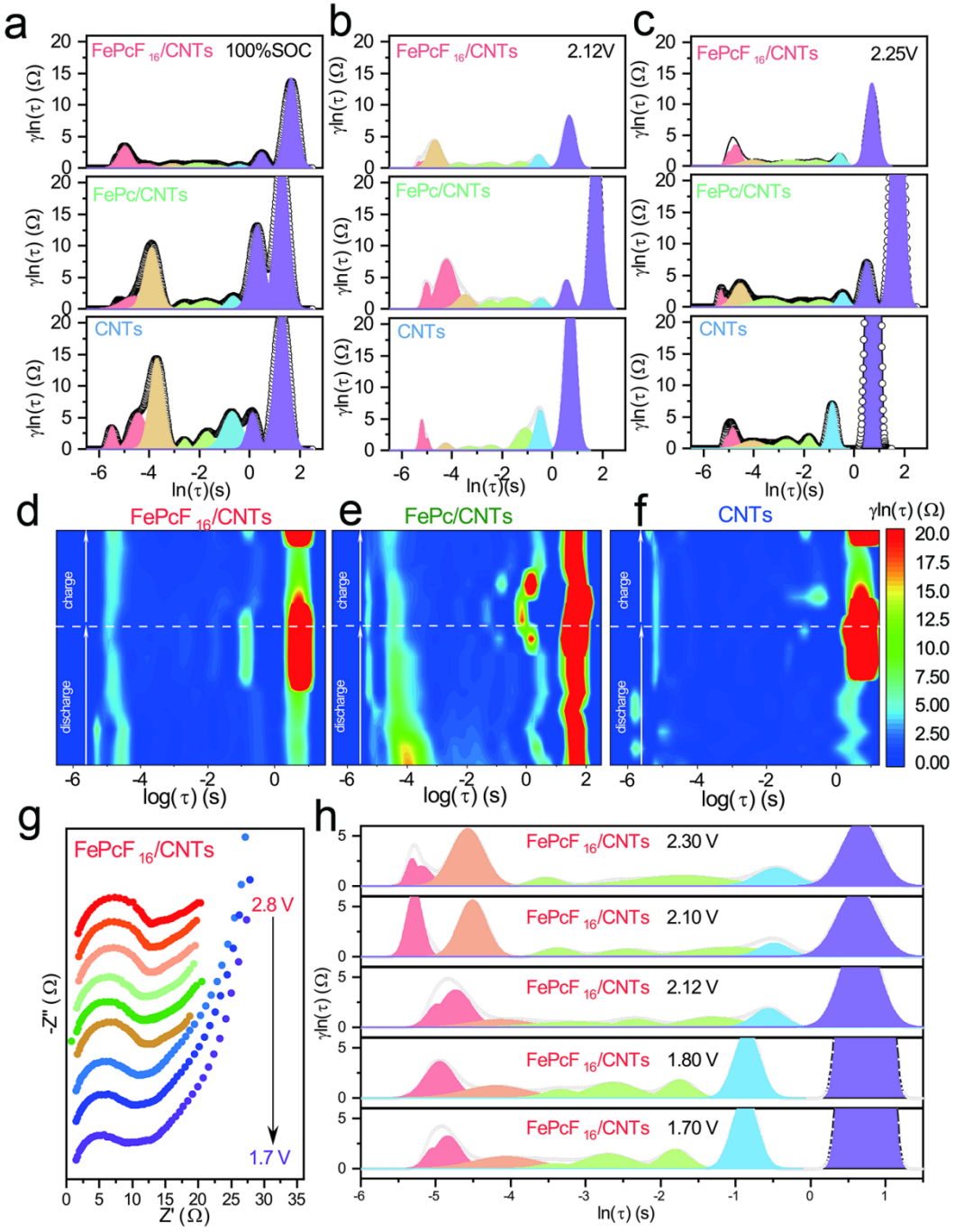

Figure 5. DRT profile corresponding of various separators at (a) 100% SOC, (b) 2.12 V and (c) 2.25 V. The 2D contour maps of (d) the $FePcF_{16}$/CNTs, (e) FePc/CNTs and (f) CNTs. (g) *In-situ* EIS spectra of the $FePcF_{16}$/CNTs in discharge process. (h) The corresponding DRT curves.

Above mentioned results could trace back to the well-dispered $FePcF_{16}$ nano-particles, with sufficient F group for boosting the nucleus density of Li_2S and then promote the transition kinetics by active central Fe-N_4 catalytic unit.

The DRT curves of the $FePcF_{16}$/CNTs, FePc/CNTs and CNTs under same charge/discharge conditions are compared to reveal the catalytic ability of the $FePcF_{16}$, detailed in Table S2 and Table S3[30,31]. At 100% SOC, the DRT profile of FePc/CNTs exhibits a reduction of all resistance, expect Li^+ diffusion resistance. And the $FePcF_{16}$/CNTs with F functional groups shows the obvious reduction in all region, especially in cathode charge transfer and diffusion region, demonstrating the FePc can reduce the inner particle resistance and improve the charge transfer efficiency in cathode. When introduce the F groups, the affinity between LiPS and Li^+ as well as the charge exchange ability are both boosted (Figure 5a).

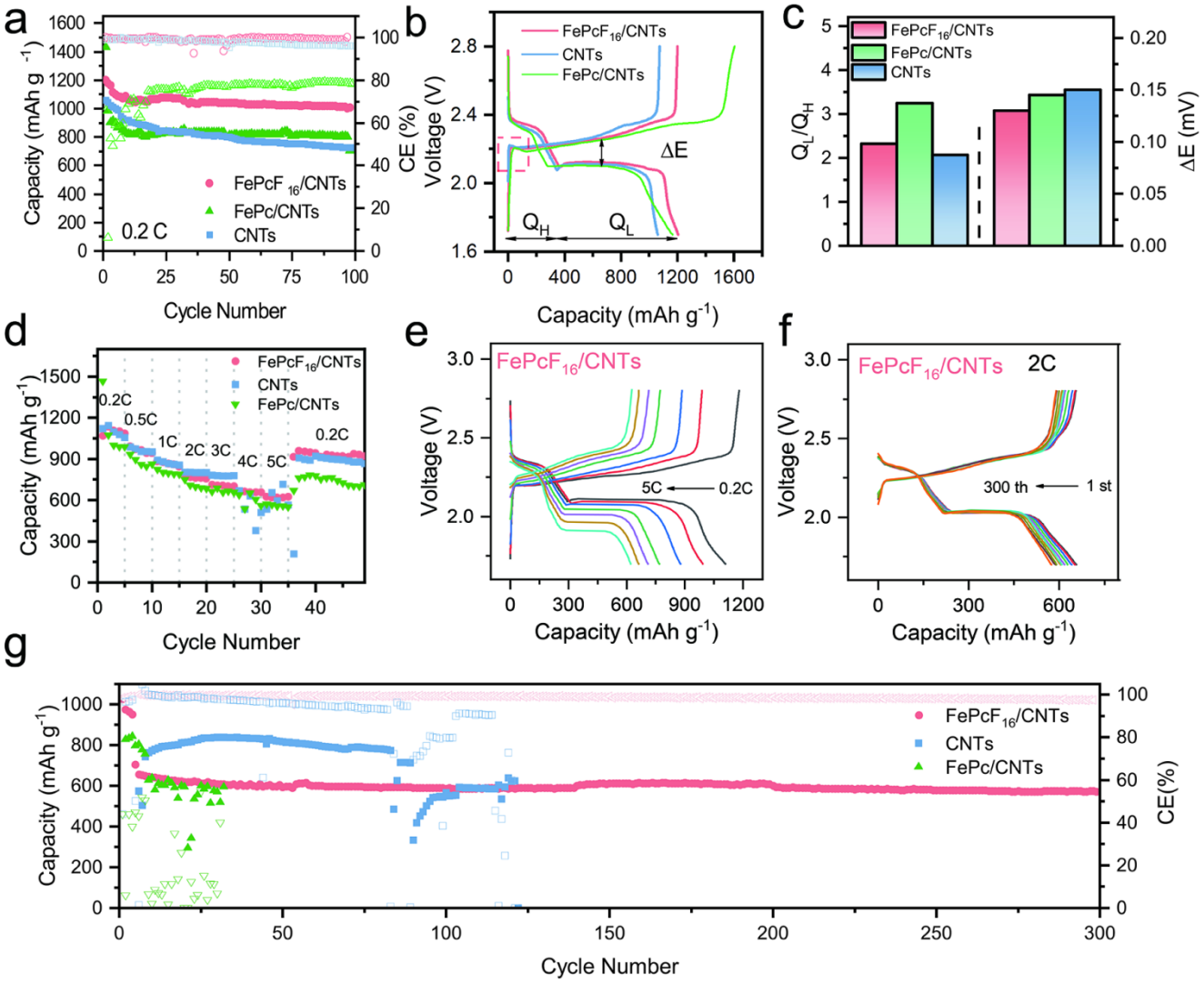

Figure 6. (a) Charge/discharge curves of the $FePcF_{16}$/CNTs, FePc/CNTs and CNTs at 0.2C. (b) Partly charge discharge curve of the $FePcF_{16}$/CNTs and CNTs at 0.2C. (c) The corresponding column value of Q_H/Q_L and ΔE at 0.2C. (d) Rate performance of the $FePcF_{16}$/CNTs and CNTs. (e) Charge/discharge curves of the $FePcF_{16}$/CNTs at rates in the range of 0.2-5C. (f) Charge/discharge curves of the $FePcF_{16}$/CNTs at various cycle numbers. (g) Long-term cycling performance of the $FePcF_{16}$/CNTs and CNTs at 2C.

The reduction of resistance may attribute to the enhanced electrolyte wettability of the strong polar F groups on the introduced $FePcF_{16}$.The raised Li^+ and LiPS migration rate also impact Li_2S nucleation mode. In Li_2S nucleation state at second discharge plateaus around 2.12 V(Figure 5b), the FePcF/CNTs separator exhibit a promoted LiPS diffusion rate than CNTs separator, which may impact the Li_2S growth model from 3DP into 2DI and greatly increase the size of Li_2S sticks(Figure 4h). For $FePcF_{16}$/CNTs cells, the Li^+ diffusion resistance decreases along with the introduce of F functional groups, accomplishing the smaller t_m value of 981 s and higher I_m value, demonstrated the $FePcF_{16}$/CNTs enabling the fastest bulk diffusion rate and the highest nucleus density. In the Li_2S activation potential at around 2.25 V(Figure 5c), there shows the same results, the FePc/CNTs can accelerate the diffusion rate of LiPS. When introduce the F functional group, the $FePcF_{16}$/CNTs catalyst displays the extra effect for Li^+ diffusion in bulk phase. The DRT profile prove that the central Fe-N_4 units of FePc exhibit strong affinity towards LiPS and the F functional group of $FePcF_{16}$/CNTs can lower Li^+ transfer resistance, enabling a fast mass migration.

The DRT curves of whole charge/discharge procedure was displayed in Figure 5d-f. The $FePcF_{16}$/CNTs delivers the lowest resistance in all three samples. To further investigate kinetics of the $FePcF_{16}$/CNTs detailed in discharge procedure, *in situ* EIS and the corresponding DRT analysis were measured (Figure 5g and Figure 5h). When discharge to 2.30 V, the S_8 in cathode converted into soluble long-chain LiPS and released to the electrolyte. This conversion breaks the dense structure of sulfur filled cathode[32], leading an increasement of P_1(ohmic resistance

τ = 3 μs), P_4(diffusion resistance of LiPS τ = 0.3 s) and P_5 (diffusion resistance of Li^+ τ = 5 s). When discharge to the start point of second plateaus around 2.10 V, the long-chain LiPS transferred into short-chain soluble Li_2S_4. The concentration of LiPS in electrolyte reaches the maximum and significantly hinder the migration of LiPS and Li^+[30]. The resistance of P_4 and P_5 also reach its maximum value in all discharge process. At the same time, the charge transfer resistance increasement may because of the dissolution of active materials. At the second plateaus at around 2.12 V, the soluble Li_2S_4 consumes and starts to precipitate on the cathode with Li_2S_2, the LiPS concentration in electrolyte reduces. The mass migration dynamics decreases along with this reaction[24]. When discharge to 1.8 V, the Li_2S_2 converted to Li_2S along with the charge transfer resistance reduces owing to the change of phase and the diffusion resistance of Li^+ reduces[30].

The cycle performance at 0.2C of various separators were shown in the Figure 6a, the cell with the $FePcF_{16}$/CNTs interlayer delivered the highest initial discharge capacity of 1204.5 mAh g^{-1} as well as a highest capacity retention of 83.68%. In comparison, the FePc/CNTs cell exhibits a severe overcharge phenomenon, indicating a low CE around 80%. The CNTs modified separator displays a fast capacity decay after 100 cycles along with lower sulfur utilization than that of the $FePcF_{16}$/CNTs, indicating the improved stability and reversibility by introducing the F functional groups.

The charge-discharge curves with separators at 0.2C were displayed in Figure 6b. The $FePcF_{16}$/CNTs separator delivered the longest plateaus in both charge and discharge process, indicating the enhanced sulfur utilization. Additionally, the $FePcF_{16}$/CNTs interlayer exhibits the lowest potential for activating the Li_2S oxidation procedure, demonstrating the reduction of the transition barrier in both Li_2S nucleation and activation (Figure S6a). The potential differences between the charge and discharge curves reflects the polarization, the $FePcF_{16}$/CNTs interlayer shows the lowest ΔV of 0.13 V, determined improvement of intrinsic charge and mass transfer kinetics, and the higher Q_L/Q_H ratio of 2.32 also exhibit a higher reversibility of redox reaction. Although the FePc/CNTs cell exhibits an ultrahigh Q_L/Q_H value, the discharge capacity of Q_H part is only 202.6 mAh g^{-1}.(Figure 6c).

Rate performances were illustrated in Figure 6d, the $FePcF_{16}$/CNTs exhibits the average reversible capacities of 1136.2, 992.5, 885.2, 779.3, 708.8 and 624.9 mAh g^{-1} at 0.2C, 0.5C, 1C, 2C, 3C, 4C and 5C, respectively. $FePcF_{16}$/CNTs cell still retained 624.9 mAh g^{-1} in 5C and the corresponding charge/discharge curve still maintain a typical shape (Figure. 6e). For comparison, CNTs shows an overcharge phenomenon in high rate of 4C and 5C(Figure S6b), confirming that the $FePcF_{16}$/CNTs interlayer can achieve rapid LiPS conversion dynamics. The FePc/CNTs show the lower capacity than CNTs and even more severe overcharge phenomenon.

The long-term cyclic performance at 2C is shown in Figure 6g. The FePc/CNTs separator shows the lowest CE around 20%, demonstrating a ultra-low cycle stability in 2C. The cell with CNTs separator displays a higher capacity than the $FePcF_{16}$/CNTs separator, which attributed to the high specific surface area and high electronic conductivity of 3D CNTs layer. However, the volumetric expansion between S and Li_2S and the dense Li_2S passivation layer cause the battery failure after about 120 cycles. The $FePcF_{16}$/CNTs separator exhibits an initial capacity of 704.6 mAh g^{-1} at 2C with a low capacity decay of 0.43‰ per cycle after 300 cycles and capacity retention of 87.63%. The charge/discharge curves at 2C delivered a stable discharge plateau voltage around 2.0 V after 300 cycles (Figure 6f). The excellent long-term performance is possibly attributed to the $FePcF_{16}$ nanoparticles which provide more active sites to anchor and catalyze LiPS conversion, affording good reversibility and stability.

Conclusions

In this work, 10 nm $FePcF_{16}$ with well exposed catalytic surface were homogenously synthesized on the surface of CNTs in solid process. The FePc/CNTs are also synthesized to insight the effect of the catalytic central $Fe\text{-}N_4$ and strong electron withdraw F substituent groups. As a result, the catalytic central $Fe\text{-}N_4$ unit exhibits strong adsorption and 'scissor' effect towards Li-S bond of LiPS in both lithiation and delithation process. Additionally, the introduce of the F functional groups further promoted the catalytic effect of $Fe\text{-}N_4$ towards LiPS as well as the Li^+ diffusion rate in bulk phase. The well dispersed $FePcF_{16}$ particles delivered a high Li_2S nucleation rate and nucleus density, enabling 3D fine particles on cathode surface and avoiding the overcharge phenomenon which possible attributed to the passivation of electrode surface. DRT analyses were used to insight the kinetics evaluation, the $Fe\text{-}N_4$ units and the introduced F functional groups could reduce the diffusion resistance of LiPS and Li ion. Consequently, the cell with $FePcF_{16}$/CNTs interlayer delivered a high initial capacity (1136.2 mAh g^{-1} at 0.2C), excellent rate performance (624.9 mAh g^{-1} at 5C) and superior long-term stability with low capacity decay after 300 cycle at 2C of 0.43‰.

Experimental Section

Synthesis of the $FePcF_{16}$/CNTs and FePc/CNTs

0.2 g of Carboxylic acid functionalized-MWCNTs (CNTs, Chengdu Organic Chemicals co., Ltd., Chinese Academy of Sciences), 0.31 g of Ammonium iron (II) sulfate hexahydrate($Fe(NH_4)_2{\cdot}(SO_4)_2{\cdot}6H_2O$, 99%, Sinopharm Chemical Reagent Co., Ltd) 0.06 g of ($(NH_4)_6Mo_7O_{24}{\bullet}4H_2O$, 99%, Sinopharm Chemical Reagent Co., Ltd), 0.6 g of urea (AR, 99% shanghai Aladdin Biochemical Technology Co., Ltd) and 0.41 g of Tetrafluorophthalic acid(AR, 99%, Tokyo chemical industry Co., Ltd) were grinded together uniformly into a powder mixture. $FePcF_{16}$/CNTs were synthesized by heating the mixture to 140°C for 30 min and then increased temperature to 270°C for 2 h. Followed by a series of purification procedure, $FePcF_{16}$/CNTs composite were obtained.

The $FePcF_{16}$/CNTs were synthesized by 0.2 g of CNTs, 0.31 g of $(Fe(NH_4)_2{\cdot}(SO_4)_2{\cdot}6H_2O$, 0.06 g of $(NH_4)_6Mo_7O_{24}{\bullet}4H_2O$,

0.6 g of urea and 0.41 g of phthalic anhydride in the same method of $FePcF_{16}$/CNTs.

Supporting Information

Supporting Information is available from the Wiley Online Library.

Acknowledgements

This work was supported by the National Natural Science Foundation of China (No. 52073166, 52172049, U22A20144); the Shaanxi Natural Science Foundation of China (No. 2019JLM-3). The special program of local service from Education Department of Shaanxi Province (22JC017), Natural Science Foundation of Shaanxi Province (2023-JC-YB-302), Natural Science Basic Research Program of Shaanxi (2022JQ-373.Acknowledgements Text.

Conflicts of Interests

There are no conflicts to declare

Author Contributions

Jiaqi Zhao: investigation, data curation, Visualization ,writing-original draft of experimental part, Writing-review & editing. Zhanwei Xu: Funding acquisition, supervision, writing-review & editing. Yujiao Zhang: writing-review & editing. Siyu Chen: conceptualization. Qingzhu Jin: validation. Longhua Guo: validation. Xuetao Shen: writing-review & editing. Jiayin Li: Funding acquisition. Zhi Li: supervision, writing-review & editing.

Data availability Statement

Research data are not shared.

Keywords: F substituent group • iron phthalocyanine • polysulfide • shuttle effect • lithium sulfur batteries

[1] a)H. Chu, J. Jung, H. Noh, S. Yuk, J. Lee, J. H. Lee, J. Baek, Y. Roh, H. Kwon, D. Choi, K. Sohn, Y. Kim,H. T. Kim, Adv. Energy Mater. 2020, 10; b)R. Meng, X. He, S. J. H. Ong, C. Cui, S. Song, P. Paoprasert, Q. Pang, Z. J. Xu,X. Liang, Angew Chem Int Ed Engl 2023, 62, e202309046; c)C. Li, K. Yang, Z. Ma, F. Zhao, J. Li, X. Xu, X. Hao, H. Qi,Y. He, J. Mater. Chem. A 2024, 12, 174-183.

[2] Q. Gong, L. Hou, T. Li, Y. Jiao,P. Wu, ACS Nano 2022.

[3] a)R. Sun, Y. Bai, M. Luo, M. Qu, Z. Wang, W. Sun,K. Sun, ACS Nano 2021, 15, 739-750; b)W. Wang, L. Huai, S. Wu, J. Shan, J. Zhu, Z. Liu, L. Yue,Y. Li, ACS Nano 2021.

[4] a)T. Wang, D. Luo, Y. Zhang, Z. Zhang, J. Wang, G. Cui, X. Wang, A. Yu,Z. Chen, ACS Nano 2021, 15, 19457-19467; b)D. Tian, X. Song, Y. Qiu, X. Sun, B. Jiang, C. Zhao, Y. Zhang, X. Xu, L. Fan,N. Zhang, ACS Nano 2021, 15, 16515-16524.

[5] C. Shang, G. Li, B. Wei, J. Wang, R. Gao, Y. Tian, Q. Chen, Y. Zhang, L. Shui, G. Zhou, Y. Hu, Z. Chen,X. Wang, Adv. Energy Mater. 2020, 11.

[6] B. Advanced MaterialsShi, Y. Wang, E. Liu, S. Mei,C.-J. Yao, J. Mater. Chem. A 2024.

[7] a)C.-C. Wu, Y.-C. Ho,S.-H. Chung, J. Mater. Chem. A 2023, 11, 24651-24660; b)B. N. Olana, S.-H. Pan, B.-J. Hwang, H. Althues, J.-C. Jiang,S. D. Lin, J. Mater. Chem. A 2024; c)R. Paste, S. Li, J.-H. Fu, Y.-H. Chiang, A. I. Inamdar, M.-H. Chiang, V. Tung, H.-C. Lin,C. W. Chu, J. Mater. Chem. A 2023, 11, 8265-8276; d)M. Li, H. Chen, Y. Wang, X. Chen, J. Wu, J. Su, M. Wang, X. Li, C. Li, L. Ma, X. Li,Y. Chen, J. Mater. Chem. A 2023, 11, 11721-11729; e)W. Yan, X. Gao, J. L. Yang, X. Xiong, S. Xia, W. Huang, Y. Chen, L. Fu, Y. Zhu,Y. Wu, Small 2022, 18, e2106679; f)S. Tian, J. Huang, H. Yang, G. Liu, Q. Zeng, D. Wang, X. Sun, K. Tao, G. Liu,S. Peng, Small 2022, 18, e2205163; g)Z. Shi, Z. Tian, D. Guo, Y. Wang, Z. Bayhan, A. S. Alzahrani,H. N. Alshareef, ACS Energy Lett. 2023, 8, 3054-3080; h)B. Wang, S. Lu, P. Zhang, X. Jiang, X. Zhao, L. Wang, Z. Yin,J. Wu, Energy Technol. 2023, 11.

[8] B. Liu, H. Gu, J. F. Torres, Z. Yin,A. Tricoli, Energy Environ. Sci. 2024.

[9] L. Sun, X. Bao, Y. Li, J. Zhao, P. Chen, H. Liu, X. Wang,W. Liu, ACS Appl. Nano Mater. 2023, 6, 11095-11103.

[10] G. Chen, X. Song, S. Wang, X. Chen,H. Wang, J. Power Sources 2018, 408, 58-64.

[11] R. Li, X. Zhou, H. Shen, M. Yang,C. Li, ACS Nano 2019, 13, 10049-10061.

[12] Y. Li, X. Zhang, Q. Zhang, J. Cui, X. Liang, J. Yan, J. Liu, H. H. Tan, Y. Yu,Y. Wu, ACS Appl Mater Interfaces 2022, 14, 18634-18645.

[13] S. Dasarathan, J. Sung, J. W. Hong, Y. S. Jo, B. G. Kim, Y. J. Lee, H. Y. Choi, J. W. Park,D. Kim, RSC Adv 2023, 13, 8299-8306.

[14] Y. Guo, Z. Jin, J. Lu, Z. Wang, Z. Song, A. Wang, W. Wang,Y. Huang, Energy Environ. Mater. 2023.

[15] a)H.-g. Wang, Q. Wu, L. Cheng, L. Chen, M. Li,G. Zhu, Energy Storage Mater. 2022, 52, 495-513; b)N. Lv, Q. Li, H. Zhu, S. Mu, X. Luo, X. Ren, X. Liu, S. Li, C. Cheng,T. Ma, Adv Sci (Weinh) 2023, 10, e2206239; c)M. Wang, Z. Zhang, H. Zhong, X. Huang, W. Li, M. Hambsch, P. Zhang, Z. Wang, P. St Petkov, T. Heine, S. C. B. Mannsfeld, X. Feng,R. Dong, Angew Chem Int Ed Engl 2021, 60, 18666-18672.

[16] A. B. Sorokin, Chem Rev 2013, 113, 8152-8191.

[17] a)J. Ma, M. Yu, J. Zhu, W. Li, W. Gong,H. Qiu, Ionics 2021, 27, 3007-3016; b)J. Xia, R. Cao,Q. Wu, RSC Adv 2022, 12, 13975-13984; c)X. Li, Z. Fu, J. Wang, X. Zhao, Y. Zhang, W. Liu, Q. Cai,C. Hu, Chem. Eng. J. 2022, 450; d)X. Li, X. Zhao, J. Wang, C. Chen,C. Hu, Carbon 2023, 201, 307-317; e)Z. Shi, K. Zhang, K. Xiao, X. Xing, H. Xu, L. Wang, H. Yue, Y. Yin,S. Yang, ACS Appl. Energy Mater. 2021, 4, 7743-7750; f)J. Kim, H. Shin, D. J. Yoo, S. Kang, S. Y. Chung, K. Char,J. W. Choi, Adv. Funct. Mater. 2021, 31; g)X. Zhao, Y. Zhang, W. Liu, Z. Zheng, Z. Fu, C. Chen,C. Hu, Adv. Funct. Mater. 2023.

[18] C. A. Melendres,V. A. Maroni, J. Raman Spectrosc. 2005, 15, 319-326.

[19] I. V. Klimenko, A. V. Lobanov, E. A. Trusova,A. N. Schegolikhin, Russian Journal of Physical Chemistry B 2020, 13, 964-968.

[20] R. Aroca,F. Martin, J. Raman Spectrosc. 2005, 17, 243-247.

[21] a)Y. Cao, S. C. Gu, J. W. Han, Q. H. Yang,W. Lv, Chem. Rec. 2022, 22, 22; b)H. M. Wang, H. Yuan, W. W. Wang, X. Y. Wang, J. G. Sun, J. Yang, X. M. Liu, Q. Zhao, T. Wang, N. Wen, Y. L. Gao, K. P. Song, D. R. Chen, S. J. Wang, Y. W. Zhang,J. H. Wang, Adv. Mater. 2023, 12; c)P. Zeng, H. Yu, X.

Zhou, Z. Y. Zhou, B. Li, M. F. Chen, H. B. Shu, Y. Wang, B. B. Chang, X. W. Guo,X. Y. Wang, Chem. Eng. J. 2022, 427, 10.
[22] L. Peng, Z. Wei, C. Wan, J. Li, Z. Chen, D. Zhu, D. Baumann, H. Liu, C. S. Allen, X. Xu, A. I. Kirkland, I. Shakir, Z. Almutairi, S. Tolbert, B. Dunn, Y. Huang, P. Sautet,X. Duan, Nat. Catal. 2020, 3, 762-770.
[23] Q. Y. Wu, K. Y. Chen, Z. Shadike, C. L. Li, ACS Nano. 2024, 18, 21, 13468-13483.
[24] R. Soni, J. B. Robinson, P. R. Shearing, D. J. L. Brett, A. J. E. Rettie,T. S. Miller, Energy Storage Mater. 2022, 51, 97-107.
[25] X. X. Yang, X. T. Li, C. F. Zhao, Z. H. Fu, Q. S. Zhang,C. Hu, ACS Appl Mater Interfaces 2020, 12, 32752-32763.
[26] Q. Liang, S. Wang, X. Lu, X. Jia, J. Yang, F. Liang, Q. Xie, C. Yang, J. Qian, H. Song,R. Chen, ACS Nano 2024, 18, 2395-2408.
[27] Z. Li, Y. Zhou, Y. Wang,Y.-C. Lu, Adv. Energy Mater. 2019, 9.
[28] M. E. Hyde,R. G. Compton, J. Electroanal. Chem. 2003, 549, 1-12.
[29] F. Y. Fan, W. C. Carter,Y. M. Chiang, Adv Mater 2015, 27, 5203-5209.
[30] L. Liu, Y. Meng, Y. Ge,D. Xiao, ACS Appl Mater Interfaces 2023, 15, 33525-33540.
[31] L.-P. Hou, X.-Q. Zhang, B.-Q. Li,Q. Zhang, Mater. Today 2021, 45, 62-76.
[32] Y. Lu, C.-Z. Zhao, J.-Q. Huang,Q. Zhang, Joule 2022, 6, 1172-1198.

Entry for the Table of Contents

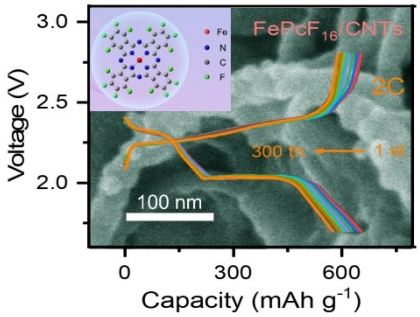

Carbon nanotube supported $FePcF_{16}$ ultrafine particulate($FePcF_{16}$/ CNTs) separators were employed for boosting Li ion migration rate and LiPS conversion kinetics due to its Strong electron withdraw group F and catalytic Fe-N_4 units. The $FePcF_{16}$/ CNTs separator exhibits a low capacity decay after 300 cycles at 2C of 0.43‰.